Characterization of the equatorial electrojet and its magnetic signatures deduced from Swarm observations

Article *in* Advances in Space Research · July 2025

DOI: 10.1016/j.asr.2025.07.031

5 authors, including:

Daphine Ayebare
Mbarara University of Science and Technology

Geoffrey Andima
Busitema University (BU)

Patrick Mungufeni
Muni University

ARTICLE IN PRESS

Available online at www.sciencedirect.com

ScienceDirect

Advances in Space Research xxx (xxxx) xxx

ADVANCES IN SPACE RESEARCH (a COSPAR publication)

www.elsevier.com/locate/asr

Characterization of the equatorial electrojet and its magnetic signatures deduced from Swarm observations

Daphine Ayebare [a,b,*], Geoffrey Andima [c], Patrick Mungufeni [d], Jean Claude Uwamahoro [e], Edward Jurua [a]

[a] *Department of Physics, Mbarara University of Science and Technology, Mbarara, Uganda*
[b] *Department of Physical sciences, Mountains of the Moon University, Fortportal, Uganda*
[c] *Department of Physics, Busitema University, Tororo, Uganda*
[d] *Department of Physics, Muni University, Arua, Uganda*
[e] *Department of Physics, University of Rwanda, Kigali, Rwanda*

Received 18 December 2024; received in revised form 7 July 2025; accepted 11 July 2025

Abstract

This paper presents a long-term comprehensive analysis of the Equatorial Electrojet (EEJ) and Counter Equatorial Electrojet (CEJ) from the Absolute Scalar Magnetometers (ASM) on the Swarm satellites, for the period of nine years (2014–2022). For the first time, the altitude-dependent characteristics of the CEJ and EEJ have been determined, and the influence of the disturbance dynamo electric field (DDEF) and prompt penetration electric field (PPEF) on CEJ occurrence rates, EEJ and Equatorial electric field (EEF) amplitudes has been investigated. Results reveal that the DDEF was more pronounced in the morning sector (07:00–12:00 LT), while an eastward PPEF was dominant in the afternoon sector (12:00–18:00 LT). The strongest EEJ magnetic signals are observed during September equinox months, while the weakest EEJ signals occur during the June solstice months. Additionally, the EEJ increases with solar activity but appears reduced from Swarm B. The gradient of the EEJ is positive from 06:00 to 10:00 LT and negative from 11:00 to 17:00 LT, with the peak value around 08:00 LT. The largest EEJ gradients are observed in January, and the smallest gradients in March. The EEJ lunar tidal modulation is greatest in December and least in June. The CEJ occurrence rates from Swarm A, B, and C exhibited a consistent pattern of lunar tidal modulation.

Keywords: Equatorial magnetic signals; Equatorial electrojet; Counter electrojet

1. Introduction

The day-time eastward equatorial electric field (EEF) in the ionospheric E-region is responsible for driving many equatorial electrodynamics (Alken et al., 2015). This EEF is created through a dynamo action, where the thermospheric neutral winds cause the charged particles to move across the magnetic field lines, resulting in an eastward electric field (Alken and Maus, 2007). At low latitudes, the nearly horizontal northward geomagnetic field lines are mutually perpendicular to the EEF, and this drives the vertical plasma drift, until the polarization charges accumulate due to the low conducting boundaries above and below the E region (Onwumechili, 1997; Forbes, 1981; Heelis, 2004). The polarization electric field is greater than the primary EEF that causes it, leading to an

* Corresponding author at: Department of Physics, Mbarara University of Science and Technology, Mbarara, Uganda.
E-mail address: ayebaredaphine@gmail.com (D. Ayebare).

https://doi.org/10.1016/j.asr.2025.07.031

Please cite this article as: D. Ayebare, G. Andima, P. Mungufeni et al., Characterization of the equatorial electrojet and its magnetic signatures deduced from Swarm observations, Advances in Space Research, https://doi.org/10.1016/j.asr.2025.07.031

enhanced eastward conductivity beyond the normal Pedersen conductivity (Abdu, 1992; Hajra et al., 2009; Martyn, 1948). This enhanced effective cowling conductivity near the magnetic equator gives rise to the Equatorial electrojet (EEJ) (Cowling, 1932).

The EEJ is a strip of current flowing in the Ionospheric E region, within about ±3° latitudes from the geomagnetic equator, and is usually eastward during daytime (Reddy, 1981; Habarulema et al., 2019; Yizengaw et al., 2014; Rabiu et al., 2013). The EEJ presents as enhancements in the measured diurnal variation of the horizontal component (H) of the geomagnetic field near the magnetic dip equator (Anderson et al., 2002). It was first measured at the Huancayo geomagnetic observatory in Peru in 1922 (Chandra, 2000; Le Mouël et al., 2006). It also produces magnetic signatures in Low Earth Orbiting (LEO) satellites. These EEJ magnetic signatures appear to be negative with a sharp depression at the geomagnetic equator, when extracted at the altitude of LEO satellites (Cain and Sweeney, 1973). This is because the LEO satellites fly above the EEJ current, and create an induced magnetic field which is opposite to the main field. The EEJ produces a strong induced magnetic field which is northward below its peak altitude (about 110 km), and southward in the region above its peak (Onwumechili and Agu, 1981). This induced magnetic fields in turn cause a strong enhancement on H component of the geomagnetic field when it is measured by magnetometers below the EEJ altitude, and a depletion on H when measured by magnetometers above its peak (Yizengaw and Groves, 2018).

Sometimes, the EEJ is reversed to the westward direction, a phenomena named counter electrojet (CEJ) as first proposed by Gouin (1967). The reason for this reversal during quiet periods has been attributed to the westward zonal winds, atmospheric gravity waves, lunar tides amplification during stratospheric sudden warming (SSW), vertical upward winds, and quasi-biennial oscillation (Somayajulu et al., 1993; Vineeth et al., 2012; Sastri and Arora, 1981; Raghavarao and Anandarao, 1980; Chen et al., 1995). Another contribution of the reversal comes from high magnetic activity. During the northward turning of the interplanetary magnetic field (IMF B_z), the shielding electric fields dominate and convection electric field decreases. This leads to the reversal of the electric fields at mid and low latitudes (Rastogi and Patel, 1975; Fejer et al., 1979; Kobea et al., 2000; Kikuchi et al., 2000; Kikuchi et al., 2003). The westward shielding electric fields develop in the inner magnetosphere due to azimuthal gradient of plasma pressure, a condition known as overshielding of the electric field (Kelley et al., 1979; Gonzales et al., 1979). This causes a westward prompt penetration electric field (PPEF) on the day-side and an eastward PPEF disturbances on night-side ionosphere (Rastogi and Patel, 1975; Kikuchi et al., 2008). The westward PPEF appears as CEJ at the geomagnetic equator. A few hours after a major geomagnetic activity, a disturbance wind dynamo is set up, which causes a westward electric field in the low latitude E region (Blanc and Richmond, 1980), and leads to occurrence of CEJ.

The characteristics of the CEJ and EEJ have been the subject of numerous studies using both ground-based magnetometers and LEO satellites (e.g., Rastogi, 1974; Marriott et al., 1979; Alex and Mukherjee, 2001; Rabiu et al., 2017; Cain and Sweeney, 1973; Kim and King, 1999; Ivers et al., 2003; Zhou et al., 2018; Soares et al., 2018; Lühr et al., 2012; Lühr et al., 2004; Alken and Maus, 2007; Zhang et al., 2024; Zhang et al., 2022). These studies have demonstrated the variations of the EEJ and CEJ with local time, season, longitude, moon phase, geomagnetic activity, and solar activity. For example, Lühr et al. (2004) conducted the first statistical study of the EEJ based on Challenging Mini-satellite Payload (CHAMP) scalar magnetic data. This study provided a global perspective on various EEJ characteristics, such as a strong peak at the dip equator for the noon time EEJ current profiles, the variation of peak current density with longitude, and the half-width of the EEJ was constant in time at a given longitude and independent of intensity. Alken and Maus (2007) developed a global climatological Equatorial Electrojet Model (EEJM-2) using scalar magnetic field measurements from the Ørsted, CHAMP, and Scientific Application Satellite-C (SAC–C) satellites. This model predicted the local temporal, longitudinal, and seasonal variations of the EEJ, revealing that the EEJ was weaker during solstice months compared to equinox months and peaked at noon time. Recently, Lühr et al. (2021) provided a detailed overview of the climatological characteristics and tidal features of the EEJ and CEJ, based on previous studies using CHAMP observations. Zhou et al. (2018) conducted a comprehensive analysis of the CEJ and its tidal characteristics using CHAMP data, demonstrating its dependence on local time, seasons, longitude, moon phase, and both magnetic and solar activity.

The magnetic signatures of the EEJ have been studied using CHAMP observations. For instance, Doumouya and Cohen (2004) investigated the longitudinal variation of EEJ magnetic signatures around noon and showed that EEJ signatures were stronger in the Asian sector than in the African and American sectors. Benaissa et al. (2017) also examined the longitudinal and seasonal characteristics of EEJ magnetic signatures. They found that the EEJ signals were strongest during winter and spring, with the weakest signals observed during the solstice summer. Yizengaw and Groves (2018) studied the EEJ magnetic signatures using Swarm A and Swarm B observations. The study revealed a clear longitudinal dependence, with the strongest EEJ signatures observed in the West American and Asian sectors, and the weakest in the African sector. Additionally, the EEJ at Swarm A altitude was found to be significantly stronger than that at Swarm B altitude. However, the study was not long term, as it focused on a single month of October 2015 for the analysis of the EEJ signatures, which is insufficient to capture the seasonal variations of the EEJ magnetic signatures at Swarm altitudes.

Moreover, most long-term studies of the EEJ and CEJ have primarily relied on CHAMP satellite data, the Swarm satellite constellation comprising of Swarm B and a side-by-side pair, Swarm A and Swarm C offers the advantage of simultaneous multi-point observations. This unique configuration enables a more detailed characterization of the EEJ and CEJ, such as the investigation of EEJ longitudinal gradients and the altitude dependence of their characteristics. Consequently, a more comprehensive understanding of EEJ and CEJ variability is achievable with the Swarm observations, which could not be fully captured by single satellite missions.

This paper aims to provide detailed characteristics of the EEJ and CEJ, derived from the ASM (Absolute Scalar Magnetometer) on board the Swarm satellites. The study demonstrated the influence of both the DDEF and PPEF on CEJ occurrences rates, EEJ and EEF amplitudes using multi-point Swarm observations. The study further determined the long-term altitude characteristics of the EEJ and CEJ in relation to solar activity, longitudinal gradients, and lunar phases. In addition, the longitudinal and seasonal variations of EEJ magnetic signatures observed by Swarm A and B were analyzed. Characterizing these magnetic signatures is essential, as they can be used to determine key EEJ parameters, such as the peak current density, total forward current, and the spatial width of the current system.

This paper is organized as follows: the data and methods used in this study are described in Section 2, the results are presented and discussed in Section 3; and Section 4 sumarises the findings of this study.

2. Data and methods

2.1. Data set utilized

The European Space Agency (ESA) launched the Swarm mission as a constellation of three identical satellites, Alpha (Swarm-A), Bravo (Swarm-B), and Charlie (Swarm-C), to study the Earth's magnetic field (Friis-Christensen et al., 2006). Each satellite is equipped with two magnetometers, ASM which measures the strength of the magnetic field, and the Vector Field Magnetometer (VFM), which measures both the strength and direction of the magnetic field.

The magnetic dataset used in this study includes the Level 2 daily data products for EEJ and CEJ, derived from the Swarm satellite observations. The EEJ magnetic signatures were extracted from the Level 1b daily magnetic field data. The EEJ and CEJ datasets span the period from 2014 to 2022, whereas the detailed analysis of magnetic signatures was limited to the period from 2014 to 2015. This restriction was due to the availability of the CHAOS-7 model coefficient file, which extends up to the year 2015. All Swarm magnetic data products used in this study are accessible at ftp://swarm-diso.eo.esa.int/.

2.2. Methods

2.2.1. Derivation of EEJ and CEJ from Swarm satellites

This study utilized the Swarm satellites Level 2 daily data products which contain the Swarm satellites' derived EEJ, CEJ and EEF. The EEJ is extracted from the Level 1b scalar magnetic data measured by the ASM at a frequency of 1 Hz. Alken et al. (2015, 2013) showed the procedures of extracting EEJ from the Level 1b magnetic data. The magnetic signature obtained through this extraction are then inverted to estimate height integrated current density, providing an estimate of the actual current responsible for the observed magnetic signa. This is accomplished by using a model of line currents. This model represents the geomagnetically eastward flowing EEJ current, which reaches its peak in the E-region at about 110 km altitude (Heelis, 2004). The linear currents flow along lines of constant quasi dipole latitude spaced 0.5° apart. Each linear current is divided into 360 segments, where each segment is a straight line current spanning 1° of geographic longitude whose endpoints are positioned at 110 km altitude.

The estimated EEJ strength was defined as the peak of the current profile near the geomagnetic equator, as the EEJ current typically flows within ±3° of magnetic latitude. The CEJ was identified as the negative peak of the EEJ profile at the geomagnetic equator. Since the EEJ predominantly occurs during daytime, only Swarm satellite passes within the local time range of 06:00 to 18:00 were considered in the analysis.

2.2.2. Swarm satellites EEJ magnetic signature identification

The EEJ magnetic signatures were determined using the Level 1b daily magnetic scalar products. Near the dip equator, the EEJ magnetic signatures overlap with other signals from other sources, such as the fields due to the Earth's core, crust and magnetosphere. In order to obtain the EEJ magnetic signatures, these sources were isolated. The main field (B_{core} and B_{crust}), and the external magnetospheric field (B_{ext}), were removed using the CHAOS-7 geomagnetic field model (Finlay et al., 2015). This was done by subtracting the CHAOS-7 field model from the magnetic field measured by the Swarm satellites. The result gives the residual magnetic signatures primarily due to ionospheric currents. To identify the EEJ magnetic signatures, the contribution of the mid latitude ionospheric Sq currents were removed. This was achieved by fitting a polynomial of degree 5 on the latitudinal profile of the residual magnetic signatures excluding ±14° dip latitudes (Thomas et al., 2017). The fitted polynomial was then subtracted from the residual magnetic signatures due to ionospheric currents, in order to obtain the magnetic field signatures caused by the equatorial ionospheric currents which are the EEJ magnetic signatures. When applying the CHOAS model, we were only able to retrieve EEJ magnetic signatures for Swarm A and Swarm B.

2.2.3. The superposed epoch analysis

To identify the response of the EEJ, CEJ, and EEF to sudden increases in solar wind input, superposed epoch analysis (SEA) was used. The Newell coupling function (Newell et al., 2007) was chosen to represent the energy input from the solar wind into the ionosphere thermosphere system, and is defined as:

$$E'm = \frac{1}{3000} V_{SW}^{\frac{4}{3}} \left(\sqrt{B_y^2 + B_z^2}\right)^{\frac{2}{3}} \sin^{\frac{8}{3}}\left(\frac{\theta}{2}\right), \tag{1}$$

where V_{SW} is the solar wind speed in km/s, B_y and B_z are the y and z components of the IMF in geocentric solar magnetospheric (GSM) coordinates respectively, and θ is the IMF clock angle, defined as $\tan(\theta) = \frac{|B_y|}{B_z}$. The resulting units of the merging electric field E'_m are mV/m, making it directly comparable to the solar wind electric field.

As pointed out by Richmond et al. (2003), due to the inertia of the thermosphere, the response of thermospheric winds lags behind changes in the solar wind. This lag represents a memory effect in the magnetosphere-ionosphere-thermosphere system. To account for this, the time-integrated merging electric field E_m was used, defined as:

$$E_m(t, \tau) = \frac{\int_{t_1}^{t} E'm(t'), e^{(t'-t)/\tau}, dt'}{\int t_1^t e^{(t'-t)/\tau}, dt'}, \tag{2}$$

where $E_m(t, \tau)$ is a continuous function of time t, t_1 is chosen as 3 h prior to the epoch, and $\tau = 0.5$ h is the e-folding time of the exponential weighting function. The merging electric field E_m was computed at 15 min intervals using Eqs. (1) and (2). In the superposed epoch analysis, a sudden increase in E_m is identified as key time. In this study, a time step $t = n + 1$ was marked as a key time if $E_m(n+1) - E_m(n) > 0.7$ mV/m, indicating a significant increase in solar wind energy input. This approach has been used in previous studies (e.g., Xiong and Lühr, 2014; Xiong et al., 2015; Xiong et al., 2016; Zhou et al., 2018).

3. Results and discussion

3.1. The response of EEJ, CEJ and EEF to sudden increase in the Solar wind input

Fig. 1 presents the mean temporal variation of the merging electric field (E_m) from 3 h before to 15 h after the key time ($\Delta t = 0$), based on events from the Swarm satellites. Over the 9 year period, a total of 19,229, 19,204, and 19,419 events exhibiting sudden disturbances were detected by Swarm A, B, and C, respectively. As shown in Fig. 1, a sudden increase in E_m is observed at the key time, with values rising by about 1.3 mV/m and peaking to about 2.6 mV/m for all three satellites. This sharp increase in E_m signifies the onset of a magnetic disturbance. After this peak, E_m decreases rapidly over the next 3 h, and then more gradually until $\Delta t = 15$ hours.

This observation is similar with previous studies (e.g., Xiong et al., 2015; Xiong et al., 2016; Zhou et al., 2018). They reported a similar sudden increase in E_m at the key time, reaching peak values of about 4 mV/m based on CHAMP satellite observations.

Fig. 2 shows the monthly variation of the merging electric field (E_m) from 3 h before to 15 h after the key time ($\Delta t = 0$). E_m was computed in 15 min Δt bins for each month. A distinct increase in E_m is observed at the key time across all months, indicating a consistent response to the identified events from the Swarm satellites. Additionally, a slight seasonal dependence can be observed with smaller E_m variations during equinox months (Fig. 2). This seasonal variation is similar with the findings of Xiong et al. (2016). They reported smaller E_m variations during the early spring months from CHAMP observations.

Superposed epoch analysis was applied to the amplitudes of the EEJ and EEF derived from the Swarm observations. Since each Swarm satellite provides only a single snapshot of the EEJ and CEJ per orbit, the time series of EEJ and EEF amplitudes from all events were stacked with respect to the identified key times into Δt bins with a resolution of 1.5 h, and then averaged. The time resolution of 1.5 h corresponds to the orbital period of the Swarm satellites. The averaged values of EEJ and EEF in each Δt bin presents the typical behavior pf EEJ and EEF amplitudes around the key times. Error bars were calculated as the standard error of the mean, defined as the ratio of the standard deviation (σ) to the square root of the number of events (n) in each Δt bin, expressed as:

$$\text{error} = \frac{\sigma}{\sqrt{n}}$$

Since the EEJ and CEJ are daytime phenomena, the data were sorted into two local time bins, morning (07–12 LT) and afternoon (12–18 LT).

Fig. 3 shows the temporal variation of CEJ occurrence rates after a sudden increase in solar wind input at the key time. The CEJ occurrence rates were derived by applying superposed epoch analysis to both EEJ and CEJ, and expressing the number of CEJ events in each Δt bin as a percentage of the total number of EEJ and CEJ events within that Δt bin. A prominent feature in Fig. 3 is the peak in CEJ occurrence rates occurring around 3–4.5 h after the key time ($\Delta t = 0$), in both local time sectors. This increase in CEJ occurrence rates at these times is attributed to the disturbance dynamo wind, which is driven by thermospheric winds induced by Joule heating at high latitudes. The disturbance dynamo wind reaches its peak around 3 h after a sudden increase in magnetic activity, generating a westward electric field at low latitudes (Blanc and Richmond, 1980; Huang et al., 2005; Fejer and

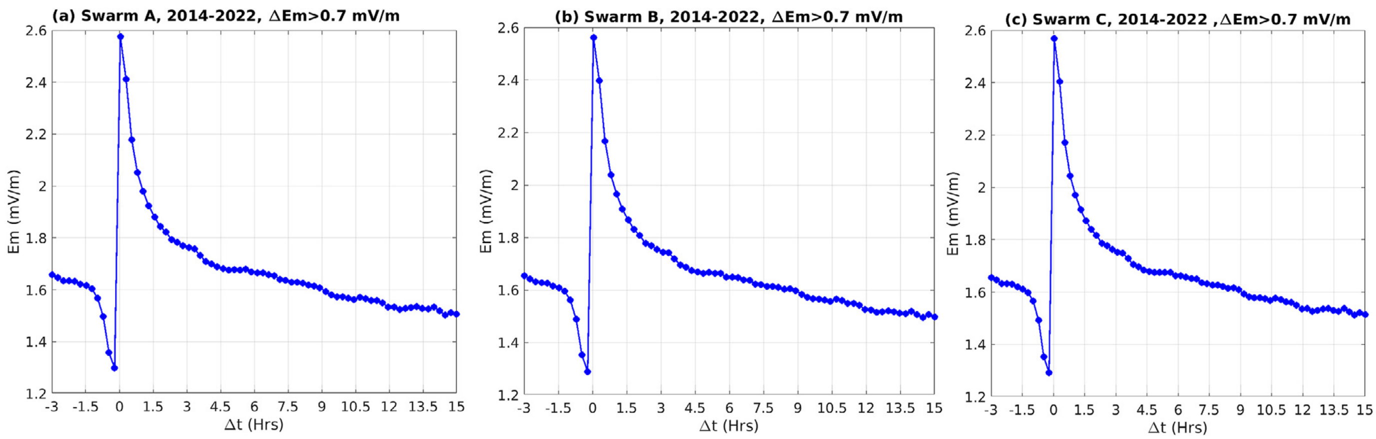

Fig. 1. Temporal variation of the merging electric field E_m from 3 h before to 15 h after the key time ($\Delta t = 0$) for the events from (a) Swarm A, (b) Swarm B and (c) Swarm C respectively.

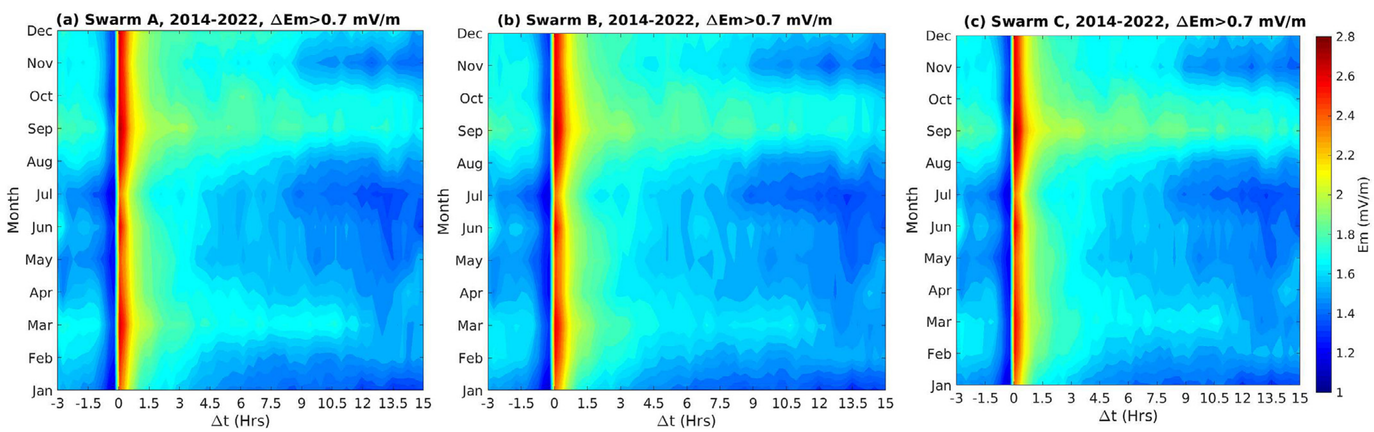

Fig. 2. Seasonal variation of the merging electric field (E_m) from 3 h before to 15 h after the key time ($\Delta t = 0$) for events from (a) Swarm A, (b) Swarm B, and (c) Swarm C, respectively.

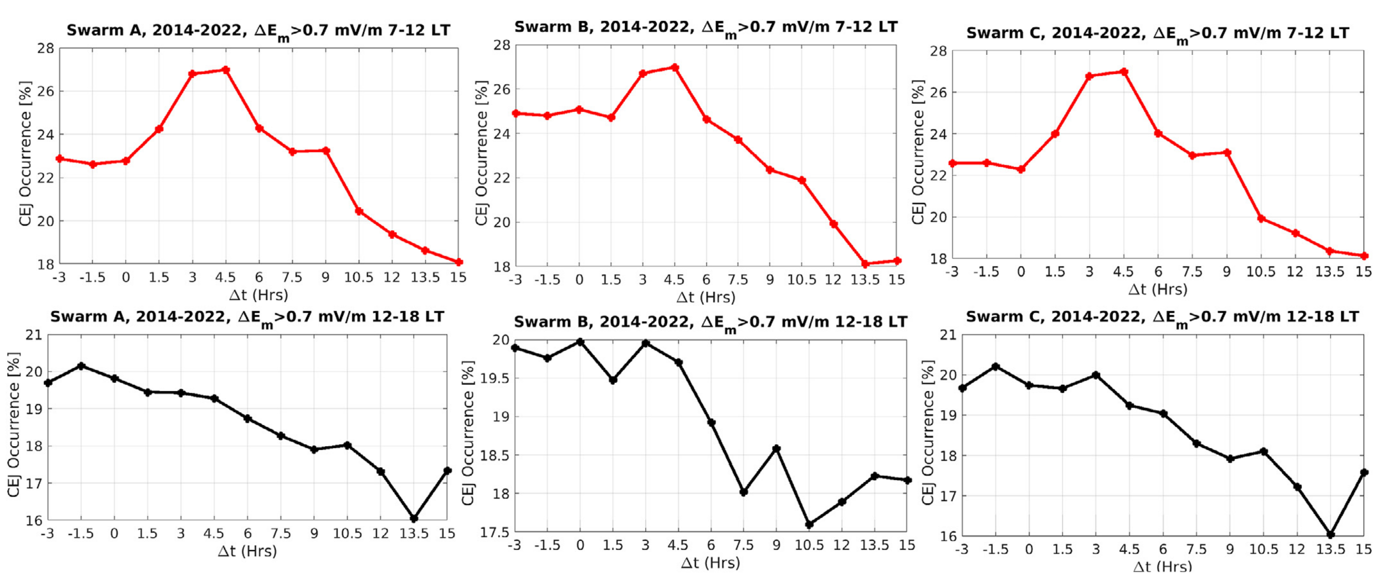

Fig. 3. Superposed epoch analysis of the CEJ occurrence rate in response to a sudden increase in solar wind input at the key time ($\Delta t = 0$), based on Swarm observations, for different local time sectors.

Scherliess, 1995), and thus enhancing the occurrence of CEJ events.

Additionally the increase of CEJ amplitudes and its occurrences rates is more pronounced during the morning time sectors as compared to the evening time sector. From 7–12 LT CEJ increases by 4%, 2% and 5% for Swarm A, B and C respectively from key time to 4.5 h, while from 12–18 LT, CEJ increases by 1% (Fig. 3). Zhou et al. (2018) reported that the local time dependence of the disturbance wind effect was comparable with the diurnal variation of CEJ occurrences from CHAMP observations.

There are also minor reductions in the CEJ occurrence rates in the evening times (12–18 LT) at around key time. After the increase in solar wind input an eastward PPEF is set up at daytime, lasting for about an hour (Zhou et al., 2018). Fig. 4 shows the temporal variation of the amplitude of the EEJ current density after a sudden increase in solar wind input. From 7–12 LT, the EEJ amplitudes are reduced at key time ($\Delta t = 0$), while from 12–18 LT, the EEJ shows an increase at key time. The increase in EEJ at key time is attributed to the transient effect of the eastward PPEF (Kikuchi et al., 1996; Kelley et al., 2003), while the decrease in EEJ at key time is associated with the westward over shielding PPEF (Kelley et al., 1979; Gonzales et al., 1979). Additionally, EEJ is generally reduced in both local time sectors from about 3 to 6 h after the key time, after which it begins to increase steadily. The reduction in EEJ during this time is related to the influence of the westward disturbance dynamo wind (Blanc and Richmond, 1980; Huang et al., 2005).

Fig. 5 shows the temporal variation of EEF amplitudes after a sudden increase in solar wind input. In both local time sectors, the EEF decreases from about 1.5 to 4.5 h after key time, with the depressions being more pronounced in the morning sector (7–12 LT) (Fig. 5). This reduction is attributed to disturbances in the EEF during geomagnetic disturbances, as the background electric field is perturbed by the westward DDEF from high latitudes (Blanc and Richmond, 1980; Huang et al., 2005). Xiong et al. (2016) also reported smaller amplitudes of the disturbed electric field observed by Republic of China Satellite 1 (ROCSAT-1) during daytime.

A minor increase in the EEF is observed around key time between 12–18 LT, which is related to the transient effect of the eastward PPEF (Kikuchi et al., 1996; Kelley et al., 2003). This result is consistent with the earlier observation of increased EEJ amplitudes (Fig. 4) and reduced CEJ occurrence rates (Fig. 3) in this local time sector.

3.2. Variation of EEJ with solar activity

The dependence of the EEJ on solar activity was analyzed during geomagnetically quiet days (Kp $\leqslant$3) to avoid any potential coupling between magnetic and solar activity. The smoothed solar flux index (P10.7) was used as an indicator of solar activity, as it provides a more accurate representation of solar activity (Liu et al., 2006). The P10.7 index is calculated using the following expression:

$$\mathrm{P10.7} = \frac{\mathrm{F10.7} + \mathrm{F10.7A}}{2},$$

where F10.7A represents the 81-day running average of the daily F10.7 value.

EEJ amplitudes from the Swarm satellites were sorted into P10.7 bins and averaged over the September equinox months (September to November), as EEJ amplitudes are greatest during the equinox (Yizengaw et al., 2014; Soares et al., 2018; Ayebare et al., 2023). Fig. 6 shows the variation of EEJ amplitudes from the Swarm satellites with solar activity for the years 2014–2022. It is clear from

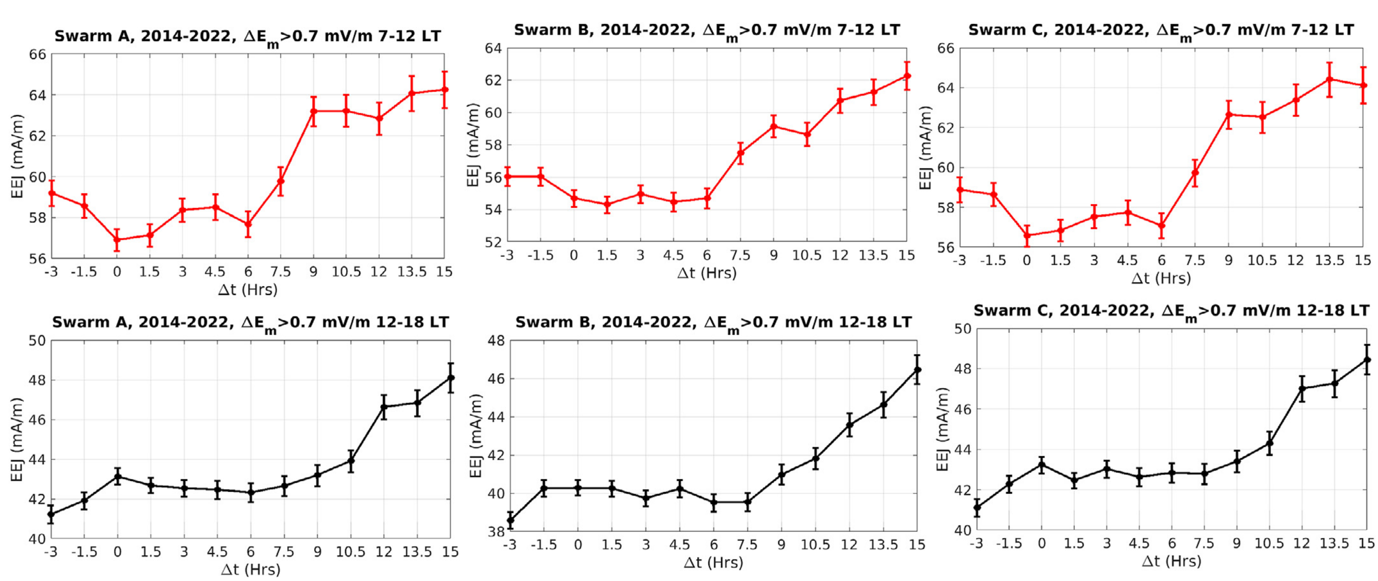

Fig. 4. Superposed epoch analysis of the amplitude of EEJ current density in response to a sudden increase of solar wind input at the key time ($\Delta t = 0$) from the Swarm observations for the different local time sector.

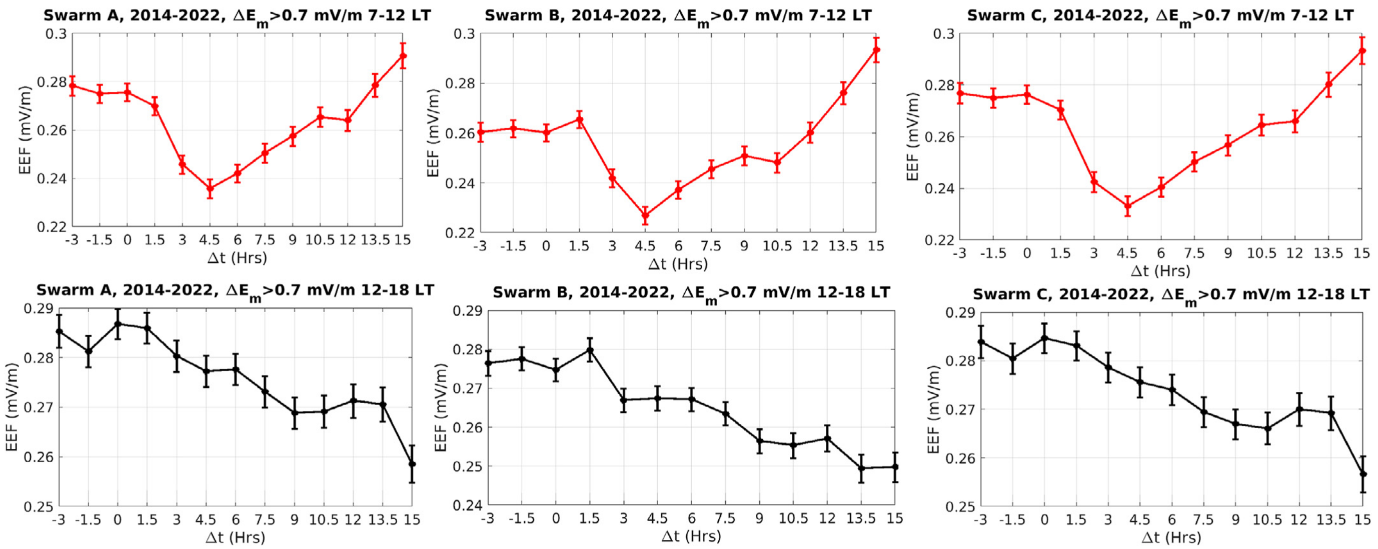

Fig. 5. Superposed epoch analysis of the amplitude of the EEF in response to a sudden increase of solar wind input at the key time ($\Delta t = 0$) from the Swarm observations for the different local time sector.

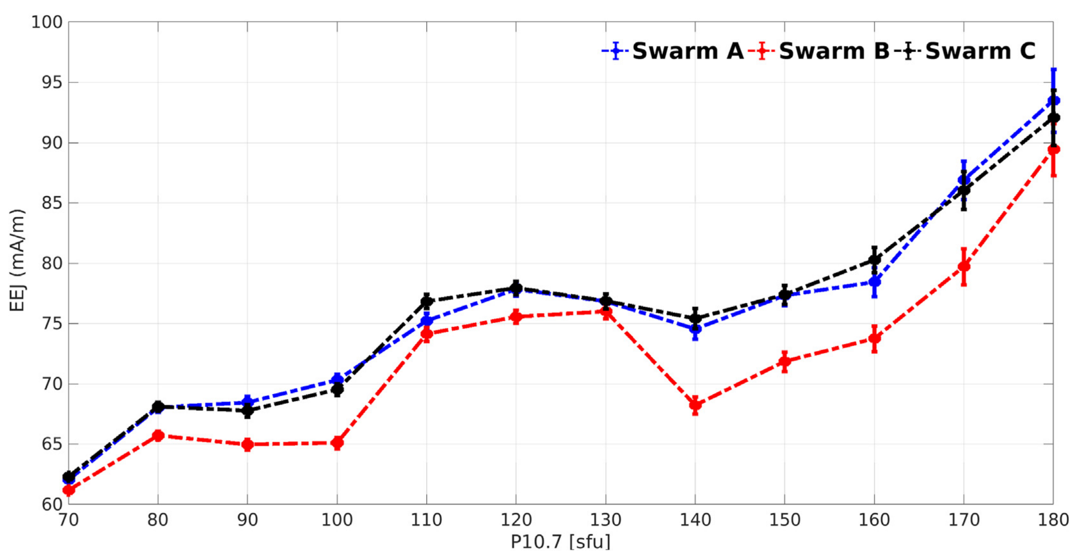

Fig. 6. Variation of EEJ from Swarm observations with the solar flux index P10.7 from 2014–2022.

Fig. 6 that EEJ amplitudes from Swarm observations generally increase with the P10.7 solar flux index. This is because ionospheric conductivity increases with P10.7. A similar observation by Lühr et al. (2021) reported a continuous increase in EEJ amplitudes from CHAMP observations as P10.7 values increased. Additionally, Alken and Maus (2007) found that the EEJ intensity varies approximately as the square root of P10.7 based on the EEJM.

However, the EEJ amplitudes observed by Swarm B are reduced compared to those from Swarm A and C (Fig. 6). This difference is attributed to the higher orbital altitude of Swarm B (about 530 km), in contrast to the lower altitudes of Swarm A and C (about 460 km).

Similarly, Yizengaw and Groves (2018) reported significantly stronger EEJ signatures at Swarm A altitude than at Swarm B altitude. Additionally, Onwumechili and Agu (1980) using magnetometer data from the Polar Orbiting Geophysical Observatories (POGO) series (OGO 2, OGO 4, and OGO 6) that were orbiting at different altitudes, reported that EEJ signature does not simply decrease with altitude but instead oscillates exhibiting enhanced EEJ signatures at specific altitudes. They observed that the EEJ signatures increased between 400–480 km and 560–620 km, but decreased between 480–560 km and 620–700 km, and subsequent increase again between 700–800 km. They attributed the oscillatory behavior of the EEJ signatures with altitude to additional localized currents layers flowing above the EEJ altitude (at 110 km). These currents are weak to produce a noticeable magnetic field on the Earth's surface but become observable as the satellite passes through them.

There is a sudden decrease of EEJ amplitudes as P10.7 increases from 130 to 140. We suggest that the observed decrease in EEJ amplitudes may be influenced by localized current systems above the EEJ peak (about 110 km). This effect appears more pronounced in Swarm B observations, possibly due to its higher orbital altitude (about 530 km), which may make it more sensitive to such high altitude current variations. Further investigation is required to confirm this explanation.

3.3. Longitudinal and seasonal variation of EEJ magnetic signatures

Fig. 7 shows a typical EEJ magnetic signature derived from Swarm B observation on 22 June 2015 during its pass over 100° W longitude at 12:54 LT. The magnetic signature tends to attain a minimum near geomagnetic equator. To study the seasonal and longitudinal variation of EEJ magnetic signatures, the data was categorized into four seasons representing March Equinox (March-May), June Solstice (June-August), September (September-November), and December Solstice (December-February). Since EEJ flows most during daytime (09:00–15:00 LT), the EEJ magnetic residuals were selected for satellite passes within the local time range 10:00–16:00 LT, during geomagnetically quiet periods from 2014 to 2015. The magnetic signatures were then sorted in bins of 2° × 5° resolution in geographic latitude and longitude, as shown in Fig. 8.

In all seasons, the EEJ magnetic signatures observed by Swarm A and B are strongest over the South American and Asian regions, and weakest over the African region (Fig. 8). Additionally, the EEJ magnetic signatures are greatest during the September equinox months, while the weakest signals are observed during the June solstice months (Fig. 8).

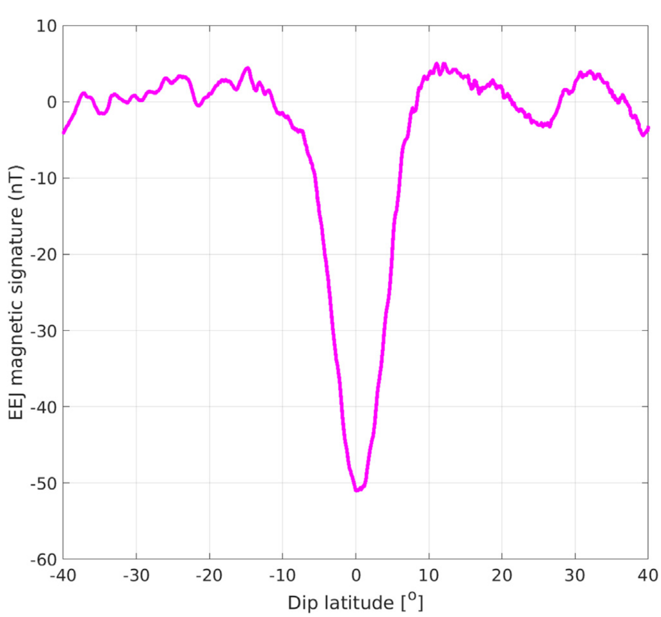

Fig. 7. The EEJ magnetic signature derived from Swarm B observation on 22 June 2015.

The seasonal and longitudinal variation of the EEJ magnetic signatures are explained interms of the effect of non-migrating tides, migrating tides and stationary planetary waves. The dominant propagating solar non migrating tide, named diurnal eastward with wave number 3 (DE3), maximizes around months of August (Lühr and Manoj, 2013), and causes longitudinal wave-4 (WN4) patterns in satellite observations of EEJ (Lühr et al., 2008; Zhou et al., 2016). The DE3 tide is primarily caused by the deep convection in the tropical troposphere, and propagates vertically upwards from its source, transferring its energy and momentum into the E-region ionosphere before being dissipated (Lühr et al., 2008; Hagan and Forbes, 2002; Hagan et al., 2007).

Additionally, Lühr et al. (2021) attributed the large amplitudes of EEJ over South America to enhanced ionospheric conductivity. The magnetic field strength is weakest over South America, and both Hall and Pedersen conductivities are inversely proportional to the magnetic field strength. The secondary peak of EEJ over East Asia is related to the large zonal electric field in that sector (Alken and Maus, 2010). Similar seasonal and longitudinal variations of EEJ magnetic signals has been reported (e.g. Benaissa et al., 2017; Yizengaw and Groves, 2018; Doumouya and Cohen, 2004).

3.4. Longitudinal gradient of EEJ

Swarm A and C fly side by side with a longitudinal separation of 1.4°, allowing them to probe the ionosphere simultaneously (Friis-Christensen et al., 2006). This configuration provides an opportunity to determine the longitudinal gradient of the EEJ over a separation of 1.4°. The EEJ gradient per 1.4° was calculated using the following equation:

$$\Delta EEJ = EEJ_C - EEJ_A,$$

where EEJ_A is the EEJ obtained from Swarm A, observed at an earlier local time, and EEJ_C is the EEJ obtained from Swarm C, observed approximately six minutes later than Swarm A. The ΔEEJ values were sorted into longitude, local time, and seasonal bins, and then averaged during quiet geomagnetic periods (Kp $\leqslant$3) from 2014 to 2022.

Fig. 9a shows the longitudinal variation of ΔEEJ, exhibiting four peaks in its structure, which represent the longitudinal wave-4 (WN4) pattern in ΔEEJ. Zhou et al. (2016) reported that the propagating tidal components, diurnal eastward with wave number 3 (DE3), diurnal westward with wave number 5 (DW5), semidiurnal westward with wave numbers 3, 4, and 6 (SW3, SW4, SW6), and planetary semidiurnal westward with wave numbers 1, 2, and 4 (SPW1, SPW2, SPW4) contribute to the WN4 structure of ΔEEJ.

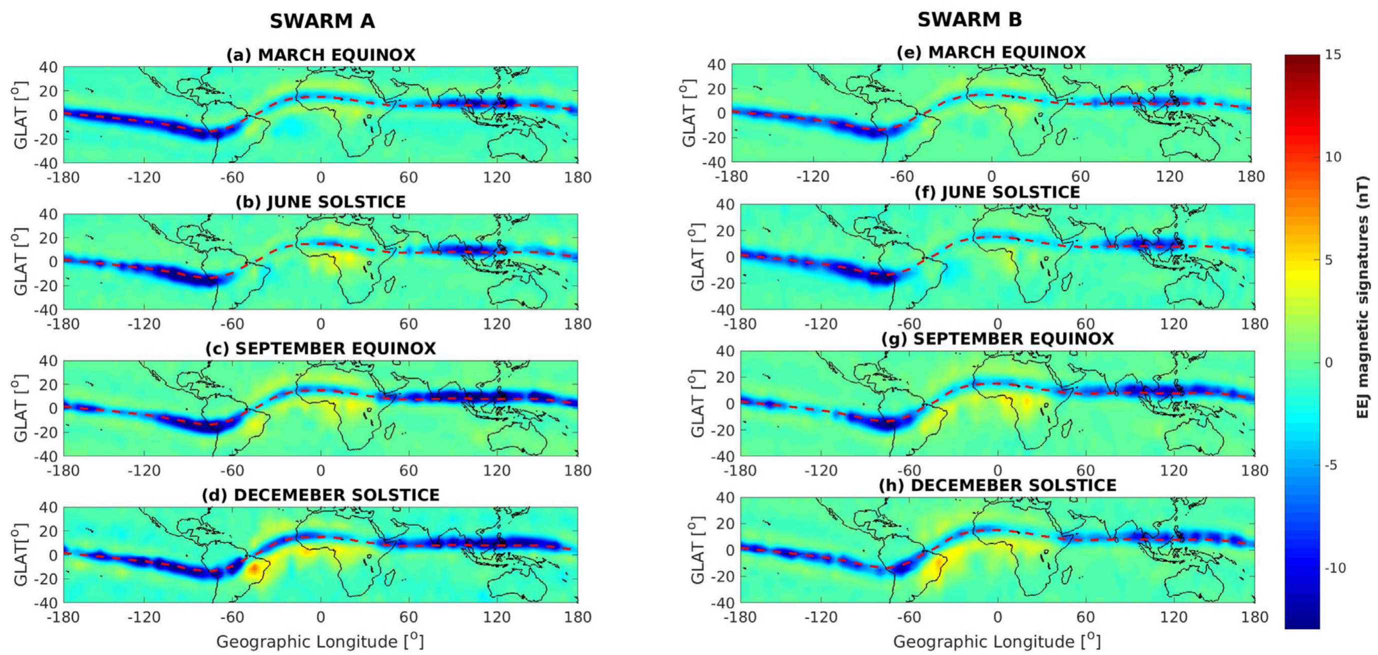

Fig. 8. The longitudinal and seasonal variation of the EEJ magnetic signatures from 10:00–16:00 LT observed by Swarm A and B during four seasons from 2014–2015. The red dotted line represents the magnetic equator.

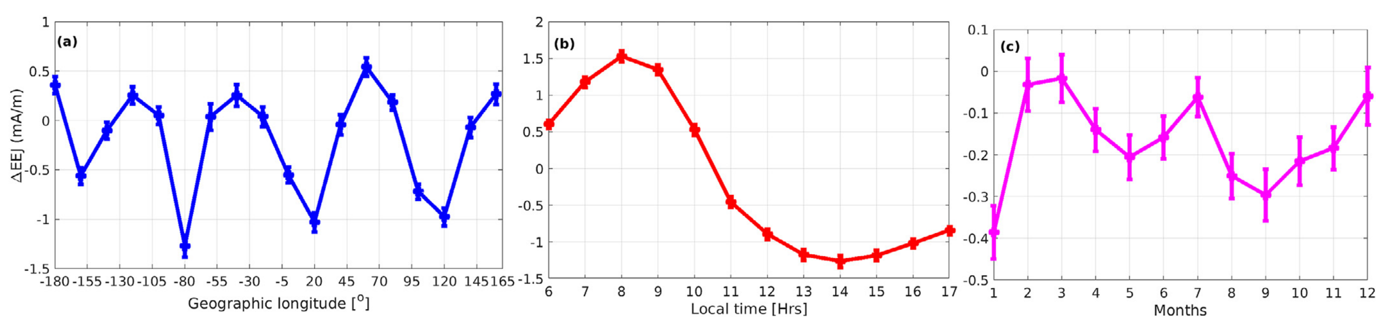

Fig. 9. The (a) longitudinal, (b) diurnal and (c) seasonal variations of EEJ gradient from 2014–2022.

ΔEEJ shows a clear local time variation, with positive values indicating an increase in the EEJ, and negative values indicating a decrease. As seen in Fig. 9b, ΔEEJ is mainly positive from 06:00 to 10:00 LT, with peak values around 08:00 LT, and turns predominantly negative from 11:00 to 17:00 LT. The negative values after 11:00 LT imply that the EEJ in the E region stops increasing beyond noon. Alex and Mukherjee (2001) reported an increase in the eastward electric field and large gradients in ionospheric conductivity around noon, consistent with this behavior. Similarly, Zhou et al. (2016) observed that ΔEEJ rises steeply between 07:00 and 09:00 LT, reaching its maximum around 10:00 LT, and switches from positive to negative near 12:00 LT.

ΔEEJ also exhibits a clear seasonal dependence, as shown in Fig. 9c. The largest ΔEEJ values are observed in January, while the smallest occur around March. As stated earlier, Zhou et al. (2016) reported the presence of several propagating tidal components SW3, SW4, SW6, DW5, DE3, SPW1, SPW2, and SPW4 contribute to the longitudinal pattern of ΔEEJ. Additionally, Lühr and Manoj (2013) showed that the second-largest non-migrating semidiurnal tide (SW4) peaks around December and January, while the non-migrating semidiurnal tide (SW3) has its largest amplitudes from October through December.We therefore suggest that the interference between these two semidiurnal westward tidal components (SW3 and SW4) during the December solstice months could explain the largest ΔEEJ observed in January.

3.5. Moon phase variation of EEJ and CEJ

The atmospheric lunar tide is a well-known source of ionospheric variability (Yamazaki et al., 2017). It is a global-scale oscillation of the Earth's atmosphere caused by the gravitational force of the moon (Lindzen and Chapman, 1969). Swarm observations were used to investigate the moon phase dependence of the EEJ and CEJ

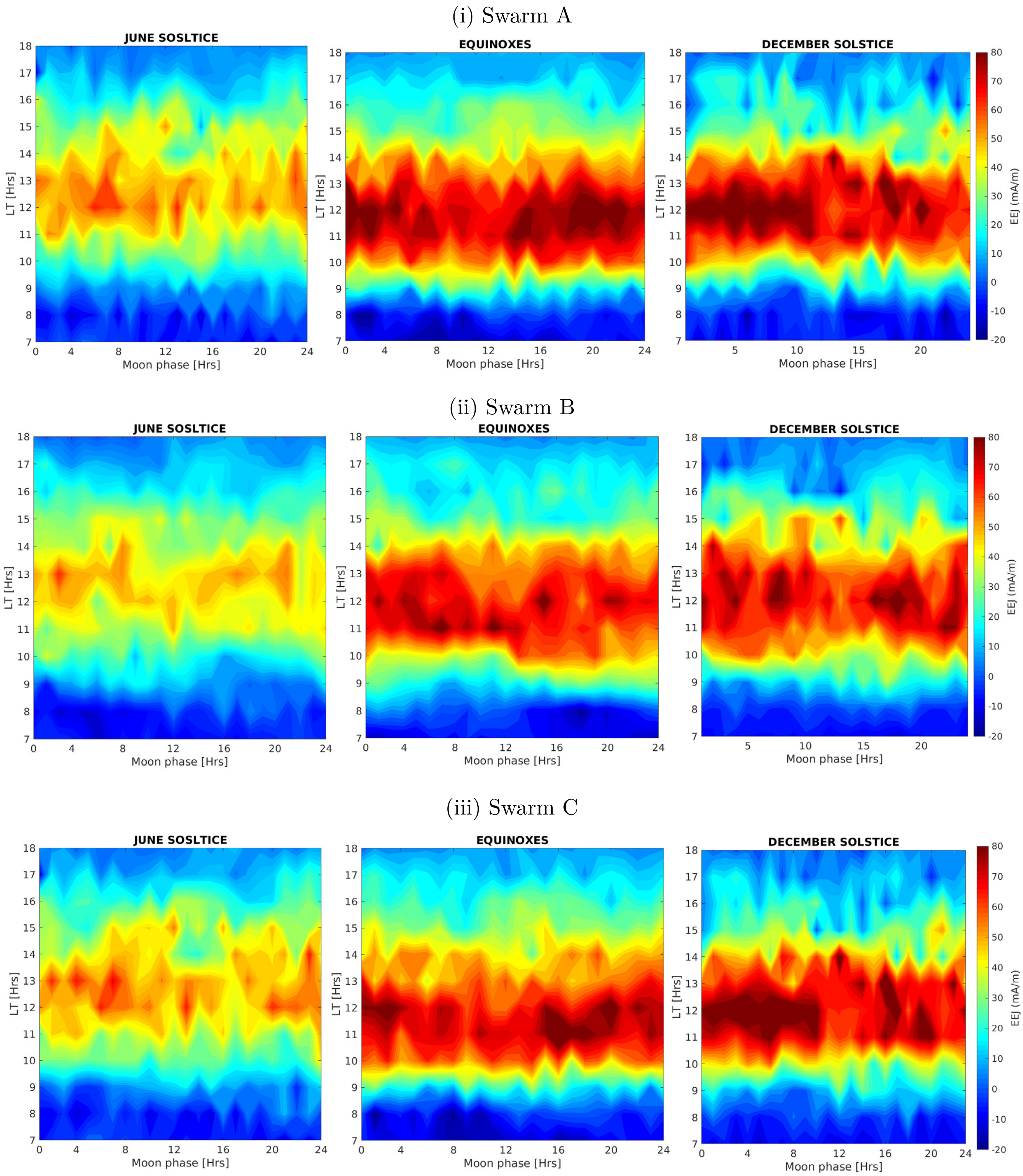

Fig. 10. Local time against moon phase hour variation of EEJ from Swarm observations from 2014–2022.

during quiet periods (Kp⩽3). The lunar phase, denoted as v, ranges from 0 to 24 h, with $v = 0$ and $v = 12$ representing the new moon and full moon, respectively. For each day, the value of v was calculated using the formula (Fanselau and Sugiura, 1966):

$$v = v_m - v_s,$$

where v_m and v_S are the moon's and sun's mean longitudes given by the equation;

$$v_m = 283.612983^\circ + 13.176396730246^\circ \tau_d + 0.00198^\circ T^2,$$

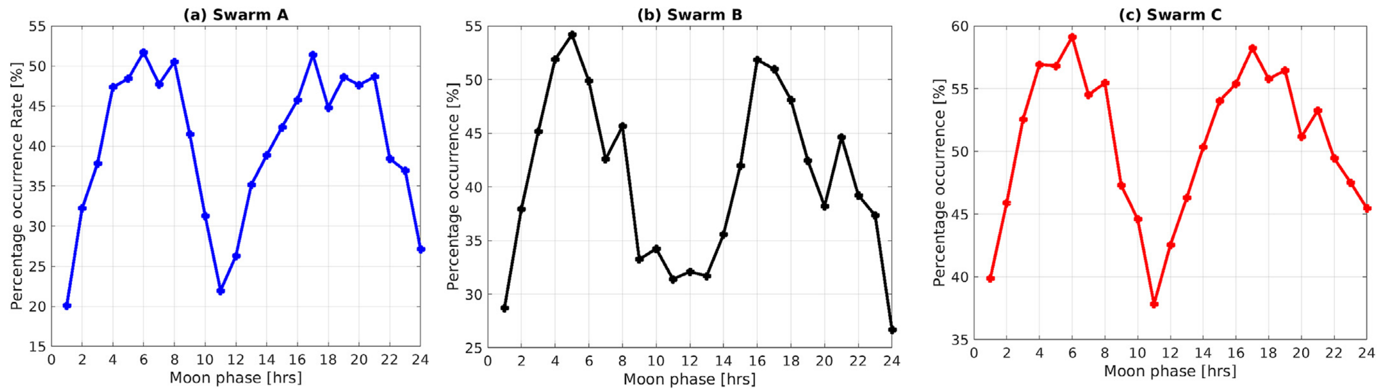

Fig. 11. Percentage occurence of CEJ with moon phase obtained from (a) Swarm A, (b) Swarm B and (c) Swarm C observations from 2014–2022.

$$v_s = 280.682325^\circ + 0.985647335387^\circ \tau_d + 0.00030^\circ T^2,$$

where, τ_d is the number of days since 12 h Greenwich Mean Time on January 1, 1900, and T is time in Julian centuries.

The EEJ from Swarm observations was calculated in 1 h bins for each lunar phase hour across different seasons, with the results shown in Fig. 10. The EEJ data were categorized into three of Lloyd's seasons: December Solstice (November to February), June Solstice (May to August), and the combined Equinoxes (March, April, September, and October). Lunar tides observed in the Swarm data cause enhancements in the EEJ at certain local times, with peaks occurring from 11:00 to 14:00 LT. The modulation of EEJ amplitude by lunar tides is largest during the December solstice months, while the smallest tidal amplitudes occur during the June solstice months. Lühr et al. (2012) reported the largest lunar modulation of EEJ from CHAMP observations during the December solstice months, attributing this to Sudden Stratospheric Warming (SSW) events, which are responsible for enhancing lunar tidal amplitudes around the December solstice. Other studies (e.g. Fejer et al., 2010; Park et al., 2012; Siddiqui et al., 2015; Yamazaki, 2013; Yamazaki et al., 2012) have also reported amplification of lunar tidal variations in EEJ during SSW events. An SSW event is a large-scale meteorological disturbance in the middle atmosphere, typically occurring in the Arctic region during winter (Andrews et al., 1987; Labitzke and Van Loon, 2012).

The dominant component of the lunar tide, known as the semidiurnal lunar tide (M_2), is generated near the Earth's surface and propagates to higher altitudes. The M_2 tide peaks at about 110 km altitude, above which the wave is damped due to molecular dissipation (Yamazaki et al., 2017). Sudden Stratospheric Warming (SSW) events create favorable conditions for the vertical propagation of the M_2 tide from the lower to the upper atmosphere, leading to the amplification of the M_2 tide (Forbes and Zhang, 2012).

The percentage occurrence rate of CEJ were calculated for each lunar phase v by dividing the number of CEJ detected events by the total number of EEJ and CEJ events in that lunar phase hour. The results of the CEJ occurrence rates for each lunar phase hour from the Swarm observations are shown in Fig. 11. Since CEJ occurrences are highest in the morning hours, the CEJ occurrences were taken from 6:00–9:00 LT.

The CEJ occurrence rates exhibit primary peaks at 06, 05, and 06 moon phase hours for Swarm A, B, and C respectively, and secondary peaks at 17, 16, and 17 moon phase hours for Swarm A, B, and C respectively (Fig. 11). Zhou et al. (2018) reported that CEJ occurrence rates observed by CHAMP also peaked shortly after the new moon (around 05 h) and full moon (around 17 h). These peak locations are attributed to the constructive interference between the solar migrating tides and the lunar semidiurnal M_2 tide, which amplifies near the crest of the M_2 tide. Similarly, Soares et al. (2018) found that the morning time CEJ occurrence rates, from ground based magnetometers over the Brazilian and Peruvian sectors, were more frequent around 06 and 18 moon phase hours.

4. Conclusion

In this study, we analyzed the long-term altitude characteristics of the EEJ and CEJ over a 9 year period (2014–2022) using Swarm observations. We examined the effects of both the DDEF and PPEF on the occurrence rates of CEJ, EEJ and EEF amplitudes. The results show that the disturbance wind dynamo effect was more prominent in the morning sector (7:00–12:00 LT) than in the afternoon sector (12:00–18:00 LT). Additionally, prominent eastward PPEF was observed in the afternoon local time sector (12:00–18:00 LT). The EEJ magnetic signatures were greatest in the South American and Asian sectors, while the weakest EEJ signatures are found in the African sector. The greatest EEJ magnetic signatures occur during the September equinox months, while the weakest signatures were observed during the June solstice. The EEJ increases with solar activity, but its amplitude was reduced for Swarm B due to its higher orbital altitude. The EEJ gradient was positive from 06:00 to 11:00 LT and negative from 12:00 to 18:00 LT, with peak values around 08:00 LT. The largest EEJ gradients occur in January, while the smallest gradients were observed in March. The EEJ amplitudes are modulated by lunar tides, with the largest modulations observed during the December solstice and the smallest during the June solstice. The CEJ occurrence rates exhibited a consistent pattern of lunar tidal modulation, with primary peaks at 06, 05, and 06 moon phase hours for Swarm A, B, and C, respectively, and secondary peaks at 17, 16, and 17 moon phase hours.

Declaration of Competing Interest

The authors declare that they have no known competing financial interests or personal relationships that could have appeared to influence the work reported in this paper.

Acknowledgments

This work was financially supported by the Swedish International Development Agency (SIDA) through the International Science Program (ISP) of the Uppsala University, Sweden. We are thankful to ESA for providing the Swarm data, which is available at ftp://swarm-diso.eo.esa.int/. The Kp index and F10.7 data used in this study were obtained from https://omniweb.gsfc.nasa.gov/.

References

Abdu, M., 1992. The international equatorial electrojet year. Eos, Trans. Am. Geophys. Union 73, 49–54.

Alex, S., Mukherjee, S., 2001. Local time dependence of the equatorial counter electrojet effect in a narrow longitudinal belt. Earth, Planets and Space 53, 1151–1161.

Alken, P., Maus, S., 2007. Spatio-temporal characterization of the equatorial electrojet from CHAMP, Ørsted, and SAC-C satellite magnetic measurements. J. Geophys. Res.: Space Phys. 112.

Alken, P., Maus, S., 2010. Electric fields in the equatorial ionosphere derived from CHAMP satellite magnetic field measurements. J. Atmos. Solar Terr. Phys. 72, 319–326.

Alken, P., Maus, S., Chulliat, A., Vigneron, P., Sirol, O., Hulot, G., 2015. Swarm equatorial electric field chain: first results. Geophys. Res. Lett. 42, 673–680.

Alken, P., Maus, S., Vigneron, P., Sirol, O., Hulot, G., 2013. Swarm SCARF equatorial electric field inversion chain. Earth, Planets and Space 65, 1309–1317.

Anderson, D., Anghel, A., Yumoto, K., Ishitsuka, M., Kudeki, E., 2002. Estimating daytime vertical E × B drift velocities in the equatorial f-region using ground-based magnetometer observations. Geophys. Res. Lett. 29, 37-1–37-4.

Andrews, D.G., Holton, J.R., Leovy, C.B., 1987. Middle atmosphere dynamics. Int. Geophys. Ser. 40.

Ayebare, D., Andima, G., Mungufeni, P., Jurua, E., 2023. Validation of equatorial electrojet derived from Swarm observations using ground based magnetometers. Adv. Space Res. 71, 3346–3356.

Benaissa, M., Berguig, M., Doumbia, V., Bouraoui, S., 2017. The equatorial electrojet (EEJ) current deduced from CHAMP satellite and ground magnetic measurements in West Africa. Arab. J. Geosci. 10, 329.

Blanc, M., Richmond, A., 1980. The ionospheric disturbance dynamo. J. Geophys. Res.: Space Phys. 85, 1669–1686.

Cain, J., Sweeney, R., 1973. The POGO data. J. Atmos. Terr. Phys. 35, 1231–1247.

Chandra, H., RG, R., 2000. Equatorial electrojet studies from rocket and ground measurements. Earth, planets and space, 52, 111–120.

Chen, P.R., Luo, Y., Ma, J., 1995. The QBO modulation of the occurrence of the counter electrojet. Geophys. Res. Lett. 22, 2717–2720.

Cowling, T.G., 1932. Magnetism, solar: the electrical conductivity of an ionised gas in the presence of a magnetic field. Mon. Not. R. Astron. Soc. 93, 90.

Doumouya, V., Cohen, Y., 2004. Improving and testing the empirical equatorial electrojet model with CHAMP satellite data. Ann. Geophys. 22, 3323–3333.

Fanselau, G., Sugiura, M., 1966. Lunar phase numbers nu and nu' for years 1850 to 2050. NASA Goddard Space Flight Center,.

Fejer, B., Olson, M., Chau, J., Stolle, C., Lühr, H., Goncharenko, L., Yumoto, K., Nagatsuma, T., 2010. Lunar-dependent equatorial ionospheric electrodynamic effects during sudden stratospheric warmings. J. Geophys. Res.: Space Phys. 115.

Fejer, B.G., Gonzales, C., Farley, D., Kelley, M., Woodman, R., 1979. Equatorial electric fields during magnetically disturbed conditions 1. The effect of the interplanetary magnetic field. J. Geophys. Res.: Space Phys. 84, 5797–5802.

Fejer, B.G., Scherliess, L., 1995. Time dependent response of equatorial ionospheric electric fields to magnetospheric disturbances. Geophys. Res. Lett. 22, 851–854.

Finlay, C.C., Olsen, N., Tøffner-Clausen, L., 2015. DTU candidate field models for IGRF-12 and the CHAOS-5 geomagnetic field model. Earth, Planets and Space 67, 114.

Forbes, J.M., 1981. The equatorial electrojet. Rev. Geophys. 19, 469–504.

Forbes, J.M., Zhang, X., 2012. Lunar tide amplification during the January 2009 stratosphere warming event: observations and theory. J. Geophys. Res.: Space Phys. 117.

Friis-Christensen, E., Lühr, H., Hulot, G., 2006. Swarm: a constellation to study the Earth's magnetic field. Earth, Planets and Space 58, 351–358.

Gonzales, C., Kelley, M., Fejer, B.G., Vickrey, J., Woodman, R., 1979. Equatorial electric fields during magnetically disturbed conditions 2. implications of simultaneous auroral and equatorial measurements. J. Geophys. Res.: Space Phys. 84, 5803–5812.

Gouin, P., 1967. On the possible existence of a counter electrojet at magnetic equatorial latitudes. Ann. Geophys. 23, 41–47.

Habarulema, J.B., Lefebvre, G., Moldwin, M.B., Katamzi-Joseph, Z.T., Yizengaw, E., 2019. Counter-electrojet occurrence as observed from C/NOFS satellite and ground-based magnetometer data over the African and American sectors. Space Weather 17, 1090–1104.

Hagan, M.E., Forbes, J.M., 2002. Migrating and nonmigrating diurnal tides in the middle and upper atmosphere excited by tropospheric latent heat release. J. Geophys. Res.: Atmos. 107.

Hagan, M.E., Maute, A., Roble, R.G., Richmond, A.D., Immel, T.J., England, S.L., 2007. Connections between deep tropical clouds and the Earth's ionosphere. Geophys. Res. Lett. 34.

Hajra, R., Chakraborty, S., Paul, A., 2009. Electrodynamical control of the ambient ionization near the equatorial anomaly crest in the Indian zone during counter electrojet days. Radio Sci. 44, 1–13.

Heelis, R., 2004. Electrodynamics in the low and middle latitude ionosphere: a tutorial. J. Atmos. Solar Terr. Phys. 66, 825–838.

Huang, C.-M., Richmond, A., Chen, M.-Q., 2005. Theoretical effects of geomagnetic activity on low-latitude ionospheric electric fields. J. Geophys. Res.: Space Phys. 110.

Ivers, D., Stening, R., Turner, J., Winch, D., 2003. Equatorial electrojet from Ørsted scalar magnetic field observations. J. Geophys. Res.: Space Phys. 108.

Kelley, M., Fejer, B.G., Gonzales, C., 1979. An explanation for anomalous equatorial ionospheric electric fields associated with a northward turning of the interplanetary magnetic field. Geophys. Res. Lett. 6, 301–304.

Kelley, M.C., Makela, J.J., Chau, J.L., Nicolls, M.J., 2003. Penetration of the solar wind electric field into the magnetosphere/ionosphere system. Geophys. Res. Lett. 30.

Kikuchi, T., Hashimoto, K., Kitamura, T.-I., Tachihara, H., Fejer, B., 2003. Equatorial counterelectrojets during substorms. J. Geophys. Res.: Space Phys. 108.

Kikuchi, T., Hashimoto, K.K., Nozaki, K., 2008. Penetration of magnetospheric electric fields to the equator during a geomagnetic storm. J. Geophys. Res.: Space Phys. 113.

Kikuchi, T., Lühr, H., Kitamura, T., Saka, O., Schlegel, K., 1996. Direct penetration of the polar electric field to the equator during a DP 2 event as detected by the auroral and equatorial magnetometer chains and the EISCAT radar. J. Geophys. Res.: Space Phys. 101, 17161–17173.

Kikuchi, T., Lühr, H., Schlegel, K., Tachihara, H., Shinohara, M., Kitamura, T.-I., 2000. Penetration of auroral electric fields to the equator during a substorm. J. Geophys. Res.: Space Phys. 105, 23251–23261.

Kim, H., King, S.D., 1999. A study of local time and longitudinal variability of the amplitude of the equatorial electrojet observed in POGO satellite data. Earth, Planets and Space 51, 373–381.

Kobea, A., Richmond, A., Emery, B., Peymirat, C., Lühr, H., Moretto, T., Hairston, M., Amory-Mazaudier, C., 2000. Electrodynamic coupling of high and low latitudes: Observations on may 27, 1993. J. Geophys. Res.: Space Phys. 105, 22979–22989.

Labitzke, K.G., Van Loon, H., 2012. The Stratosphere: Phenomena, History and Relevance.

Le Mouël, J.-L., Shebalin, P., Chulliat, A., 2006. The field of the equatorial electrojet from CHAMP data 24, 515–527.

Lindzen, R.S., Chapman, S., 1969. Atmospheric tides. Space Sci. Rev. 10, 3–188.

Liu, L., Wan, W., Ning, B., Pirog, O., Kurkin, V., 2006. Solar activity variations of the ionospheric peak electron density. J. Geophys. Res.: Space Phys. 111.

Lühr, H., Alken, P., Zhou, Y.-L., 2021. The equatorial electrojet. Ionosphere Dynam. Appl. 3, 281–299.

Lühr, H., Manoj, C., 2013. The complete spectrum of the equatorial electrojet related to solar tides: CHAMP observations. Ann. Geophys. 31, 1315–1331.

Lühr, H., Maus, S., Rother, M., 2004. Noon-time equatorial electrojet: Its spatial features as determined by the CHAMP satellite. J. Geophys. Res.: Space Phys. 109.

Lühr, H., Rother, M., Häusler, K., Alken, P., Maus, S., 2008. The influence of nonmigrating tides on the longitudinal variation of the equatorial electrojet. J. Geophys. Res.: Space Phys. 113.

Lühr, H., Siddiqui, T.A., Maus, S., 2012. Global characteristics of the lunar tidal modulation of the equatorial electrojet derived from CHAMP observations. Ann. Geophys. 30, 527–536.

Marriott, R.T., Richmond, A.D., Venkateswaran, S.V., 1979. The quiet-time equatorial electrojet and counter-electrojet. J. Geomagn. Geoelectr. 31, 311–340.

Martyn, D., 1948. Electric conductivity of the ionospheric D-region. Nature 162, 142–143.

Newell, P.T., Sotirelis, T., Liou, K., Meng, C.-I., Rich, F.J., 2007. A nearly universal solar wind-magnetosphere coupling function inferred from 10 magnetospheric state variables. J. Geophys. Res.: Space Phys. 112, A01206.

Onwumechili, C., Agu, C., 1980. General features of the magnetic field of the equatorial electrojet measured by the POGO satellites. Planet. Space Sci. 28, 1125–1130.

Onwumechili, C., Agu, C., 1981. Longitudinal variation of equatorial electrojet parameters derived from POGO satellite observations. Planet. Space Sci. 29, 627–634.

Onwumechili, C.A., 1997. The Equatorial Electrojet. Gordon and Breach Science Publishers.

Park, J., Lühr, H., Kunze, M., Fejer, B.G., Min, K.W., 2012. Effect of sudden stratospheric warming on lunar tidal modulation of the equatorial electrojet. J. Geophys. Res.: Space Phys. 117.

Rabiu, A.B., Folarin, O.O., Uozumi, T., Abdul Hamid, N.S., Yoshikawa, A., 2017. Longitudinal variation of equatorial electrojet and the occurrence of its counter electrojet. Ann. Geophys. 35, 535–545.

Rabiu, A.B., Nagarajan, N., Yumoto, K., 2013. Characteristics of equatorial electrojet over India determined from a thick current shell model. J. Atmos. Solar Terr. Phys. 92, 105–115.

Raghavarao, R., Anandarao, B.G., 1980. Vertical winds as a plausible cause for equatorial counter electrojet. Geophys. Res. Lett. 7, 357–360.

Rastogi, R., Patel, V., 1975. Effect of interplanetary magnetic field on ionosphere over the magnetic equator. Proc. Indian Acad. Sci.-Sect. A 82, 121–141.

Rastogi, R.G., 1974. Westward equatorial electrojet during daytime hours. J. Geophys. Res. 79, 1503–1512.

Reddy, C.A., 1981. The equatorial electrojet: a review of the ionospheric and geomagnetic aspects. J. Atmos. Terr. Phys. 43, 557–571.

Richmond, A., Lathuillere, C., Vennerstrøm, S., 2003. Winds in the high-latitude lower thermosphere: Dependence on the interplanetary magnetic field. J. Geophys. Res.: Space Phys. 108.

Sastri, N.S., Arora, B.R., 1981. Lunar modulation on the occurrence frequency of the afternoon counter-electrojet events at Trivandrum. Planet. Space Sci. 29, 1091–1094.

Siddiqui, T.A., Lühr, H., Stolle, C., Park, J., 2015. Relation between stratospheric sudden warming and the lunar effect on the equatorial electrojet based on Huancayo recordings. Ann. Geophys. 33, 235–243.

Soares, G., Yamazaki, Y., Matzka, J., Pinheiro, K., Morschhauser, A., Stolle, C., Alken, P., 2018. Equatorial counter electrojet longitudinal and seasonal variability in the American sector. J. Geophys. Res.: Space Phys. 123, 9906–9920.

Somayajulu, V.V., Cherian, L., Rajeev, K., Ramkumar, G., Reddi, C.R., 1993. Mean winds and tidal components during counter electrojet events. Geophys. Res. Lett. 20, 1443–1446.

Thomas, N., Vichare, G., Sinha, A.K., 2017. Characteristics of equatorial electrojet derived from Swarm satellites. Adv. Space Res. 59, 1526–1538.

Vineeth, C., Pant, T.K., Kumar, K.K., Jose, L., Sumod, S.G., Alex, S., 2012. Counter equatorial electrojet: analysis of the variability in daytime mesopause temperature and winds. J. Atmos. Solar Terr. Phys. 75, 115–121.

Xiong, C., Lühr, H., 2014. An empirical model of the auroral oval derived from CHAMP field-aligned current signatures–part 2. Ann. Geophys. 32, 623–631.

Xiong, C., Lühr, H., Fejer, B.G., 2015. Global features of the disturbance winds during storm time deduced from CHAMP observations. J. Geophys. Res.: Space Phys. 120, 5137–5150.

Xiong, C., Lühr, H., Fejer, B.G., 2016. The response of equatorial electrojet, vertical plasma drift, and thermospheric zonal wind to enhanced solar wind input. J. Geophys. Res.: Space Phys. 121, 5653–5663.

Yamazaki, Y., 2013. Large lunar tidal effects in the equatorial electrojet during northern winter and its relation to stratospheric sudden warming events. J. Geophys. Res.: Space Phys. 118, 7268–7271.

Yamazaki, Y., Richmond, A.D., Yumoto, K., 2012. Stratospheric warmings and the geomagnetic lunar tide: 1958–2007. J. Geophys. Res.: Space Phys. 117.

Yamazaki, Y., Stolle, C., Matzka, J., Siddiqui, T.A., Lühr, H., Alken, P., 2017. Longitudinal variation of the lunar tide in the equatorial electrojet. J. Geophys. Res.: Space Phys. 122, 12–445.

Yizengaw, E., Groves, K.M., 2018. Longitudinal and seasonal variability of equatorial ionospheric irregularities and electrodynamics. Space Weather 16, 946–968.

Yizengaw, E., Moldwin, M., Zesta, E., Biouele, C., Damtie, B., Mebrahtu, A., Rabiu, B., Valladares, C., Stoneback, R., 2014. The longitudinal variability of equatorial electrojet and vertical drift velocity in the African and American sectors. Ann. Geophys. 32, 231–238.

Zhang, K., Wang, H., Song, H., Zhong, Y., Xia, H., Sun, Y., Wang, C., 2024. The seasonal dependence of the unexpected afternoon westward equatorial electrojet during quiet time. J. Geophys. Res.: Space Phys. 129.

Zhang, K., Wang, H., Wang, W., 2022. Local time variations of the equatorial electrojet in simultaneous response to subauroral polarization streams during quiet time. Geophys. Res. Lett. 49.

Zhou, Y.-L., Lühr, H., Alken, P., Xiong, C., 2016. New perspectives on equatorial electrojet tidal characteristics derived from the Swarm constellation. J. Geophys. Res.: Space Phys. 121, 7226–7237.

Zhou, Y.-L., Lühr, H., Xu, H.-W., Alken, P., 2018. Comprehensive analysis of the counter equatorial electrojet: Average properties as deduced from CHAMP observations. J. Geophys. Res.: Space Phys. 123, 5159–5181.